

Characterization and Simulation of the H6 Secondary Beamline for Beam Spot Reduction

Luke J. Weaver¹

Supervisors: Dr. Laurie Nevay², Dr. Fabian Metzger²

Beams Department - Experimental Areas - Liaison to Experiments (BE-EA-LE)
CERN
Geneva, Switzerland
October 10, 2024

Abstract

In this work, the current configuration and limitations of the H6 Secondary Beamline in the Experimental North Area (EHN1) are discussed. Modifications to unused space in user zone PPE146 are proposed to decrease the beam spot downstream and simulations are made to model the proposed solution and predict the spot size of the beam. These predictions were compared and validated with measurements of the beam taken in early August 2024.

¹Department of Physics, Lehigh University, Bethlehem, PA 18015, USA

²BE-EA-LE, European Organization for Nuclear Research (CERN), Geneva, Switzerland

Contents

1	Introduction	1
1.1	Motivation	1
1.2	Theory	2
2	Methodology	4
2.1	Methodical Accelerator Design (MAD-X)	4
2.2	Monte Carlo Simulation (with BDSIM)	4
3	Configuration	4
3.1	Magnets	4
3.2	Parameter Space	4
3.3	Final Design	8
4	Modeling	10
4.1	Verification	10
4.2	Predictions & Simulation Results	12
4.3	Modification Simulation	14
5	Experimental Results	15
5.1	Taking Data	15
5.2	Comparisons	16
5.3	Emittance	17
6	Summary and Outlook	19

1 Introduction

1.1 Motivation

The H6 beamline is a high-energy, high-resolution secondary beamline located in the North Area at Experimental Hall North 1 (EHN1). This beamline provides users with hadron, muon, or electron beams within the energy range of $10\text{--}205\text{ GeVc}^{-1}$ with which to run experiments or test novel sensors. To create the beam that the H6 secondary beamline receives, a 400 GeVc^{-1} proton beam from the Super Proton Synchrotron is collided with a beryllium target (“T4”) in the TCC2 cavern. Consequently, secondary particles of varying species and momenta are produced and are selected by subsequent dipole magnets [4]. Before the target, dipoles are used to produce an offset and angle in the beam such that the right secondary momentum is selected for allowing it to pass through a Target Attenuator eXperimental area (TAX) which selects the desired momentum and angle. Together, the bending back and forth paired with the spectrometer-like dipoles after the target is a process called the “wobbling”. This process eliminates any extraneous particles and further refines the selection of the beam [2].

A variety of users utilize the H6 secondary beamline to run their experiments and, naturally, as science evolves so to do the requirements of the experiments. One notable example is the size of the beam spot. With the decrease in the size of silicon detectors, the *usable* fraction of the beam also decreases. Thus, it takes a longer period of time for a sensor to record the same number of “hits” as its larger predecessor. To combat this, there are two obvious solutions; (1) increase the intensity or (2) maintain the same intensity but decrease the size of the beam. Currently, the H6 secondary beamline is already at its RP (Radiation Protection) intensity limit, so the natural next step is to propose a solution to decrease the beam spot.

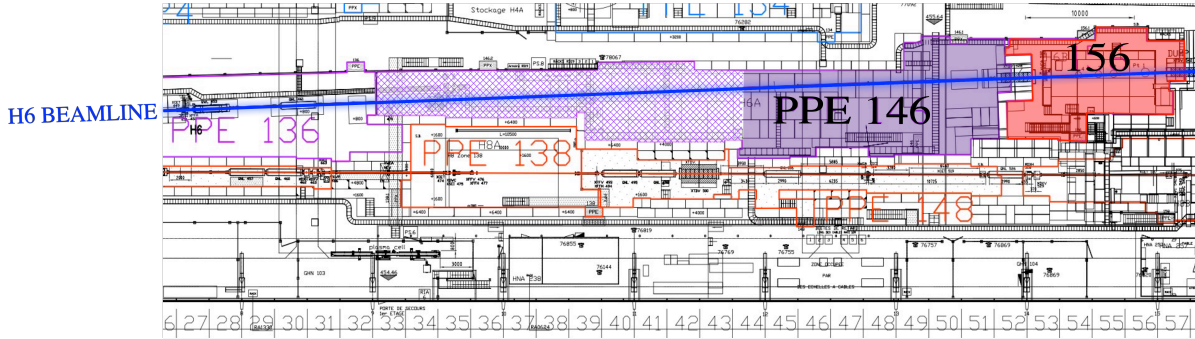


Figure 1: A diagram of the end of the H6 beamline. PPE146 (in purple) and PPE156 (in red) are shown. The usable area in PPE146 is highlighted in purple while the space unavailable for modification is crosshatched with purple.

To accomplish the task of decreasing the beam size, new quadrupole magnets can be added to focus the beam prior to the desired focus point in PPE156. To decide where to put these one can take a look at the end of PPE146. It is important to note that the last magnets are before PPE146 and so the beam from that point forward passes solely through air. Currently, a focus can only be created at the upstream part of PPE146 (to the left of Fig. 1) or in PPE156 (to the right of Fig. 1), but not concurrently. Additionally, the smallest spot size is only achievable at the very front of PPE146.

As shown in Fig. 1, highlighted in purple, is unused space in PPE146 with pre-existing wiring infrastructure where the potential quadrupole magnets could be installed. The potential exists within this area to add some new configuration of quadrupoles to further focus the beam and achieve a smaller beam spot. This avenue also provides the added benefit of outfitting the beamline with two user zones, each complete with a focus, resulting in a net increase of users and more flexibility within the line itself.

1.2 Theory

Secondary beamlines get their name - rather fittingly - from their origin. A secondary beamline is one in which primary particles are collided with a primary target, consisting of a motorized assembly of beryllium plates of varying lengths. The required beryllium plates are moved into place depending upon the user defined specifications of the beam.

Particularly, in the case of the T4 target mentioned previously, the remaining protons are transported along the ~ 1 km P42 beamline to the T10 target where a secondary beam of kaons is made for the NA62 experiment. Therefore, the choice of target length from the possible 40, 100, 180, 300, 500 mm options is a balance between sufficient transmission to P42 and sufficient secondary generation for the needs of the H6/H8 beamlines.

The resulting secondary particles produced from this collision make up the new beam (now referred to as the secondary beam). In general, a secondary beamline can be considered a transport line, and does not contain rf-cavities (radio-frequency cavities) or other accelerating components, unlike an accelerator. In addition, due to its rather chaotic origin, a secondary beamline begins its life as a diffuse beam with a generally uniform distribution. Along the beamline, the beam is filtered and molded such that it becomes a well-defined beam.

Paramount for the design of any accelerator is the use of quadrupoles and dipoles. Excluded from the previous list is higher order magnets, however, these magnets are more useful for accelerators and storage rings to combat higher order effects and so I will not touch on them here³. Dipole magnets are predominantly used for bending particle beams. This can be trivially understood on a high level by looking at the Lorentz force on a particle given by Eqn. 1.

$$\vec{F} = q\vec{v} \times \vec{B} = m\vec{a} = \frac{mv^2}{\rho} \hat{\rho} \quad (1)$$

The magnetic fields produced from the dipoles are perpendicular to the trajectory of the particle, so that the force exerted on the particle is in a circular motion in accordance with Eqn. 1. The strength of the dipole is characterized by its inverse bending radius, called its *dipole strength* κ .

In addition, quadrupole magnets are used to strongly focus the beam. When calculating the magnetic field of the quadrupole and putting it into Eqn. 1, one finds that a quadrupole will focus in one dimension, while defocusing in the other. In particular, at the centre of the quadrupole field, the field lines from each pole cancel. In the increasing transverse position, the magnitude of the field grows linearly. This acts much like an optical lens, with the important difference that it focuses in one dimension but defocuses in the other.

By using groups of quadrupole magnets, one can achieve an overall focus in both dimensions. Similarly to the dipole, quadrupoles are characterized by their *quadrupole strength* k_1 , which is the magnetic field gradient normalised to a specific magnetic rigidity given by

$$k_1 = \frac{1}{B\rho} \frac{\partial B_y}{\partial x} \quad (2)$$

where $B\rho$ is the magnetic rigidity of a given particle at a given momentum (in Tm). By convention, a positive k_1 corresponds to horizontal focusing of a positively charged particle [8].

The layout of magnets in accelerators, as well as their corresponding strengths, are often referred to as the ‘optics’. The propagation of a beam through a given set of magnets can be parameterised in two convenient forms, namely, R-Matrices and Twiss parameters. The first discussed are the R-Matrices. These matrices can be thought of as an analog to ray-transfer matrices in ray-optics [6]. By representing each element in the lattice (the beamline or accelerator optics) as a matrix which encodes a transformation of some particle coordinates moving through

³The H6 Secondary Beamline does contain a sextupole, but as previously mentioned this will be excluded from the following discussion.

the line, one can combine these matrices together to find the compound transformation of a set of particle coordinates from one position to another in a sequence of components. The canonical coordinates in a curvilinear frame that follows the nominal trajectory of the beamline (for a zero amplitude particle with the nominal momentum) are used. Amplitudes x , y are transverse spatial coordinates, and x' and y' the transverse components of normalised momentum, while δ_p is defined as $\Delta p/p_0$. These matrices will end up taking a form similar to

$$\begin{pmatrix} x \\ x' \\ y \\ y' \\ \delta_p \end{pmatrix} = \begin{pmatrix} \mathcal{R}_{11} & \mathcal{R}_{12} & \mathcal{R}_{13} & \mathcal{R}_{14} & \mathcal{R}_{15} \\ \mathcal{R}_{21} & \mathcal{R}_{22} & \mathcal{R}_{23} & \mathcal{R}_{24} & \mathcal{R}_{25} \\ \mathcal{R}_{31} & \mathcal{R}_{32} & \mathcal{R}_{33} & \mathcal{R}_{34} & \mathcal{R}_{35} \\ \mathcal{R}_{41} & \mathcal{R}_{42} & \mathcal{R}_{43} & \mathcal{R}_{44} & \mathcal{R}_{45} \\ \mathcal{R}_{51} & \mathcal{R}_{52} & \mathcal{R}_{53} & \mathcal{R}_{54} & \mathcal{R}_{55} \end{pmatrix} \begin{pmatrix} x_0 \\ x'_0 \\ y_0 \\ y'_0 \\ \delta_{p0} \end{pmatrix}$$

Similarly, the Twiss parameters come from solving Hill's equation for the motion of the particles throughout the beamline. These parameters define an ellipse in phase space which evolves as the beam progresses through the lattice. This ellipse provides a natural way of defining the beam throughout the line.

The Twiss parameters are α , β , γ , where β is an amplitude function, and α is defined in Eqn. 3.

$$\alpha = -\frac{1}{2} \frac{\partial \beta}{\partial S} \quad (3)$$

The equation of the ellipse in phase space is given by,

$$\gamma x^2 + 2\alpha x x' + \beta x'^2 = \epsilon \quad (4)$$

ϵ , the emittance, corresponds to the area of distribution in phase space [12]. Commonly, the resulting beam size is a combination of the Twiss parameters representing the action of the magnetic lattice, and the emittance, an intrinsic property of the beam launched into the lattice.

As previously mentioned, the the beam has a rather uniform distribution after the TAX and wobbling station. When considering which technique to use in characterizing the beam optics, this fact is important to consider. Twiss parameters are used to describe gaussian beams, and assume Liouville's theorem of invariant emittance. Therefore, they cannot be used to represent the beam at the beginning of the beamline. So, the R-Matrices are more useful to characterize the optics at the beginning of the line. In a secondary beamline, collimators are used to successively reduce the acceptance of the line and consequently reduce the transmitted – possibly non-Gaussian – phase space. Only once the beam gets cut and filtered downstream in the lattice can we use the Twiss parameters to describe the beam as the phase space is no longer being reduced and can be considered constant. This approximation successfully represents the propagation of the beam and the location of the foci.

One of the physics processes that is important to consider in this specific beamline is that of multiple scattering. As charged particles traverse through some medium, they experience many small scattering events from interactions with the nuclei of the material due to Coulomb scattering and strong interactions in the case of hadrons - like protons and pions. For small-angle scattering, the overall scattering can be described by a Gaussian distribution. This Gaussian approximation can be modelled by an equation given by Lynch and Dahl [9]

$$\theta_0 = \frac{13.6 MeV}{\beta c p} z \sqrt{\frac{x}{X_0}} \left[1 + 0.038 \ln \left(\frac{x z^2}{X_0 \beta^2} \right) \right] \quad (5)$$

where β , p , and c are the Loentz beta factor, momentum, and the speed of light respectively. Additionally, z is the charge number of the particle being scattered, and $\frac{x}{X_0}$ is the length of the medium in units of radiation length X_0 .

In general, beamlines and accelerators are kept in vacuum, only leaving briefly to pass through the odd scintillator. The contribution of the particles scattering from this is small,

however, towards the end of H6 there exists roughly 50 m of air. This contributes on a much larger scale.

2 Methodology

2.1 Methodical Accelerator Design (MAD-X)

The Methodical Accelerator Design (MAD-X) code provides a simple way to design accelerator lattices. It is packaged with a number of functions that allow one to construct an accelerator or beamline with various constraints. One can define a lattice in MAD-X and, given initial conditions, it will calculate various useful quantities, including the Twiss parameters, dispersion, and R-Matrices [7].

Throughout this project, MAD-X was predominantly used to *match* on specific *constraints* by varying user-specified *parameters*. In other words, one can provide MAD-X with conditions they would like it to meet at a point along the line (i.e. $\alpha_x = 0$ at a focus) and parameters to vary to meet these conditions (like magnet strengths). MAD-X will subsequently tune these free parameters to meet the conditions supplied.

During this process, MAD-X was used to create idealized beams with respect to the reference trajectory and, by varying free parameters, determined the best configuration for the new quadrupoles. It is also important to note that the way in which MAD-X was used in this project is hardly exhaustive of its full capabilities.

2.2 Monte Carlo Simulation (with BDSIM)

To fully simulate the beamline and all of the physics processes involved, the Beam Delivery Simulation (BDSIM) code was utilized [11]. BDSIM uses the Geant4 toolkit to simulate the transport of particles in accelerators and the physics processes that may take place throughout the accelerator or beamline [1].

As a brief overview, BDSIM uses the Monte Carlo simulation technique, which simulates a large number of statistically independent events to estimate beam distributions and energy deposition at various points in a beamline. Unlike MAD-X, BDSIM takes into account different physics processes, including decay and scattering, which provides us with a more accurate idea at how the beam truly looks. One can determine the multi-species distribution of the beam, the beam loss, and the beam size among other things.

In this project, BDSIM was used to determine the beam spot at various points along the line. Then these results were compared with experimental measurements. With the simulation verified, the results can be used to create accurate predictions of the outcome of the proposed modification.

3 Configuration

3.1 Magnets

The first consideration to be made in determining the setup is the type of magnets to use. Of the magnets available, the QNL magnets provide us with the greatest flexibility, sporting the highest nominal peak gradient of 24.0 Tm^{-1} [5]. Some important specifications of these magnets are included in Table 3.1.

3.2 Parameter Space

In order to determine the optimal configuration for the new quadrupoles, the free parameters must be fully accounted for in the setup.

Table 1: Specifications of QNL magnet.

Parameter	Value	Unit
Peak Gradient	24.0	Tm ⁻¹
Inscribed Diameter	80	mm
Peak Current	416	A

The area of interest stretches roughly from the end of the last quadrupole (which will be referred to as “Q16”) in the current setup to the end of the beamline, covering approximately 75 m. After Q16, the user zone PPE146 stretches over 60 m. The last 20 m of PPE146 is rather empty and is the proposed area in which the quadrupoles will be added. As previously mentioned, adding quadrupoles in this area will enable the creation of two foci, one in each user zone - PPE146 and PPE156. A useful configuration would be to have a focus in both the centres of PPE146 and PPE156.

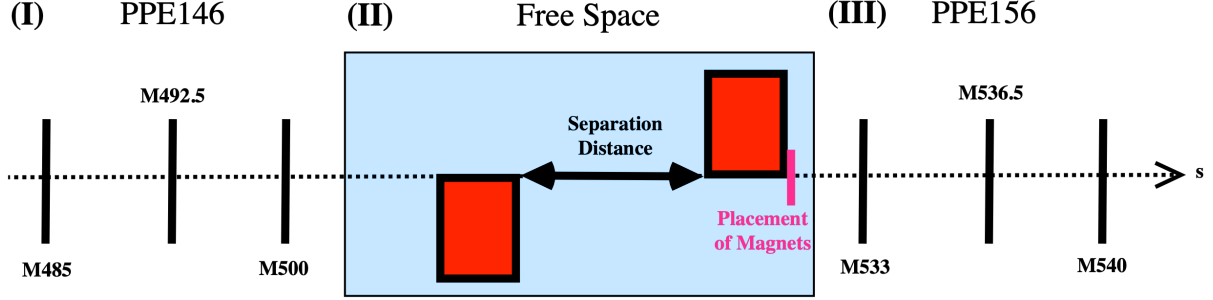


Figure 2: Schematic outline of the parameter space, demonstrating what was varied. The space where the new quadrupoles will go is sandwiched by the two user zones, in which three foci exist for each.

Fig. 2 provides a schematic outline of the procedure used, broken up into three parts. Area I and Area II are both the user zones and Area III is the free area for the quadrupoles. Within Area III one can change the number of quadrupoles installed, the space between them, and the position of the quadrupoles within the area. The goal then is to vary these parameters to find a solution to the system that allows the creation of the smallest and most symmetric beam spots throughout both user zones. It is important to note that some users may want a larger beam spot or an asymmetric beam, however, these are generally not limiting factors, and so are not included in the analysis.

So, in summary, by varying, the **position**, the **number of quadrupoles**, and the **separation distance** between the new quadrupoles one can find the smallest consecutive spot sizes in PPE146 and PPE156.

This search can be further narrowed down by considering the physics relevant in the situation. First one can consider the **position** of the quadrupoles within the free space. At this point within the line, the beam can be considered to be Gaussian. A Gaussian beam is described entirely by its beam waist and curvature radius. These parameters can be combined into a ‘complex curvature parameter’ called the q-value [6]. Given a transformation matrix

$$\mathcal{R} = \begin{pmatrix} \mathcal{R}_{11} & \mathcal{R}_{12} \\ \mathcal{R}_{21} & \mathcal{R}_{22} \end{pmatrix} \quad (6)$$

the q-value transforms according to Eqn. 7.

$$q_2 = \frac{\mathcal{R}_{11}q_1 + \mathcal{R}_{12}}{\mathcal{R}_{21}q_1 + \mathcal{R}_{22}} \quad (7)$$

Considering a simple system of a singular lens with focal length f and where both reference planes coincide with the focal planes, gives a transformation matrix of

$$\mathcal{R} = \begin{pmatrix} 1 & f \\ -\frac{1}{f} & 1 \end{pmatrix} \quad (8)$$

which combining with Eqn. 7, Eqn. 8, and rearranging, one obtains an expression for the magnification

$$\frac{w_{02}^2}{w_{01}^2} = \frac{f^2}{z_1^2 + \frac{\pi^2 w_{01}^4}{\lambda^2}} \quad (9)$$

where w_{0i} is the beam waist of the beam before and after focusing, z_1 is the distance from the initial beam waist to the lens, and λ is the wavelength - which remains constant. From this equation one can figure out how to minimize the magnification, after all the smallest beam spot possible is desired. If the focal length and initial beam waist are held constant, one clearly sees that z_1 needs to be maximized to decrease the magnification. Additionally, further insights are gained by setting the first reference plane of the system to be the lens itself. Then, one obtains the more general magnification expression Eqn. 10.

$$\frac{w_{02}^2}{w_{01}^2} = \frac{f^2}{(f - z_1)^2 + \frac{\pi^2 w_{01}^4}{\lambda^2}} \quad (10)$$

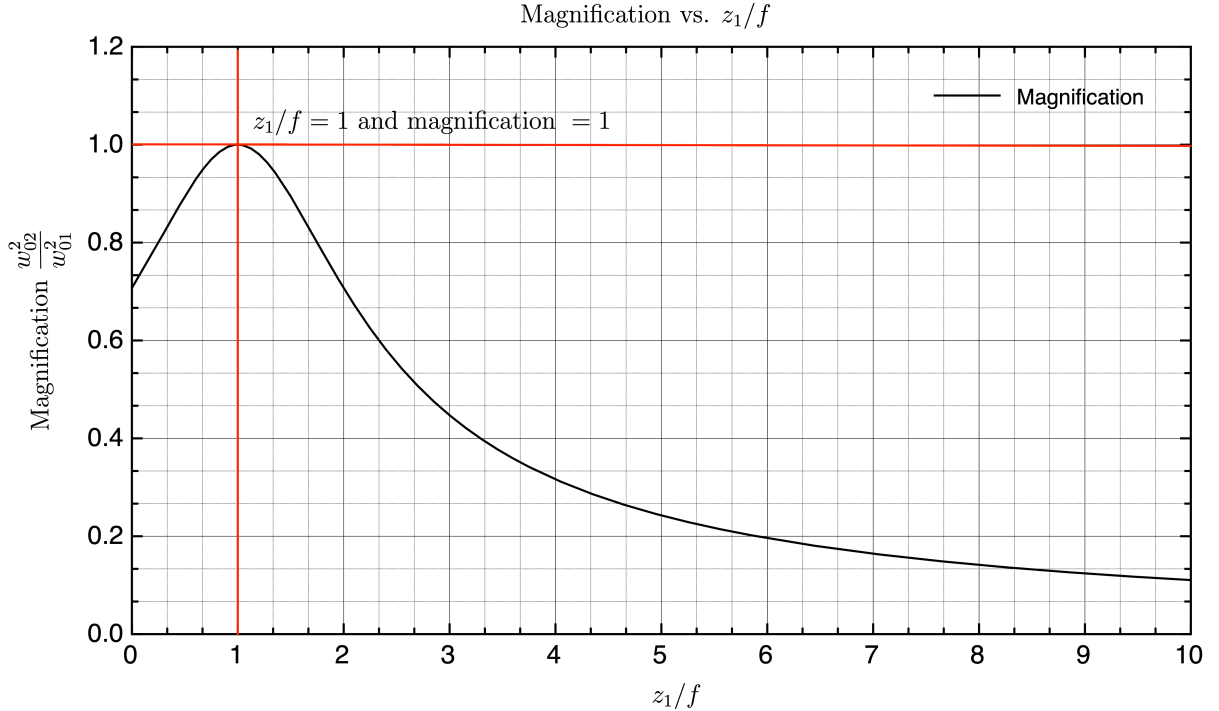


Figure 3: Magnification of a Gaussian beam at the focus as a function of the ratio of distance from original beam waist to the lens and focal length. Two regimes appear clearly, one in which the magnification increases and one in which it decreases.

Referring to Fig. 3 one can see that if the initial beam is less than the focal length, moving the beam waist further from the lens results in an increase in magnification, until it passes

the focal length, after which increasing z_1 decreases the magnification. The second regime is therefore preferable to achieve the smallest spot size.

This already simplifies the parameters, as one can look at the furthest PPE146 focal length, at 500 m, and the closest PPE156 focal length, at 532 m, and realize that the system needs to at least be past 516 m so that the second regime is active for a focus at 532 m.

If there cannot be a focus in PPE146, then a collimated beam makes the best use of the focusing strength of a quadrupole. The larger the input beam size, the smaller the focused spot size. Therefore, with no intermediate focus, a large input beam to a set of quadrupoles could be achieved with relatively small divergence.

With an intermediate focus, the input size to the new quadrupoles would depend on the location of the focus in PPE146.

In general, from this result it is clear that the quadrupoles should be placed as far from PPE146 as possible. The furthest that they can be placed in the PPE146 zone right before the vertical dump (XTDV) is at 525.58 m. To provide some room to work, the last magnet of the system is placed at 524.58 m.

Now, consider briefly the **number of quadrupoles** to use. A triplet configuration would provide the ability to create a symmetric beam throughout the entire rest of the line, while creating a comparable spot size to a doublet solution. In actuality, it is not incredibly important to maintain a symmetric beam for a long period of time, as the user experiments are not very long themselves. Additionally, it is much cheaper and requires less infrastructure to implement a doublet solution while simultaneously creating a similar spot size, so it is advantageous to use a doublet. As a result, the number of quadrupoles to use is narrowed down to two.

A Python program was created to place markers in the MAD-X sequence at regular intervals. The optical functions can only be observed at the end of elements or at markers, so these additional markers allow observation of the optical functions throughout the gap between elements. For each combination of markers, the separation between the two quadrupoles was varied from 0 m to 5 m in 0.2 m increments. For each of these separation distances, a focus is created in PPE146 at the relevant PPE146 marker by varying the strengths of Q15 and Q16. After this, a focus in PPE156 was created at the relevant marker by varying the strengths of the newly inserted magnets, Q17 and Q18. As the accepted phase space (or beam emittance) is constant at this point in the line, the Twiss parameters α_x , α_y , β_x , and β_y can be safely used to more easily match a focus. The size of the beam is dictated by

$$\sigma_i = \sqrt{\beta_i \epsilon_i + D_i^2 \left(\frac{\Delta p}{p_0} \right)^2} \quad (11)$$

where β_i , ϵ_i , D_i , and σ_p are the Twiss beta parameter, emittance, dispersion, and normalized momentum spread in the i -th dimension [12]. Therefore, to achieve a small spot size, the beta and dispersion functions should be minimised at the focus location. A focus is also defined when $\alpha = 0$ this means that the beam has achieved a focus, so α_x and α_y must both be zero at the focal point.

To investigate the optimal spacing of the two quadrupoles, Q16 and Q17 were set to give a focus in the centre of PPE146 at 492.5m. The separation was varied by changing the position of the new Q18 and Q19 in the MAD-X sequence and then matching to give a focus at 536.5m in PPE156, which will be referred to as the “nominal” setting. As shown in Fig. 4 from 0 to 2 m of separation, the size of the beam decreases. From 2 to 5 m, σ_x remains roughly constant, while σ_y increases slightly.

It remains to see how the rest of the focal combinations compare. Initially, one may expect a 1.8 m separation to be the best, however, upon inspection of the rest of the foci (as shown in Fig. 5) at 1.8 m separation, the sigma for the rest of the combinations of foci are much larger than those with a larger separation distance. These values reach a minimum at 4.2 m, after

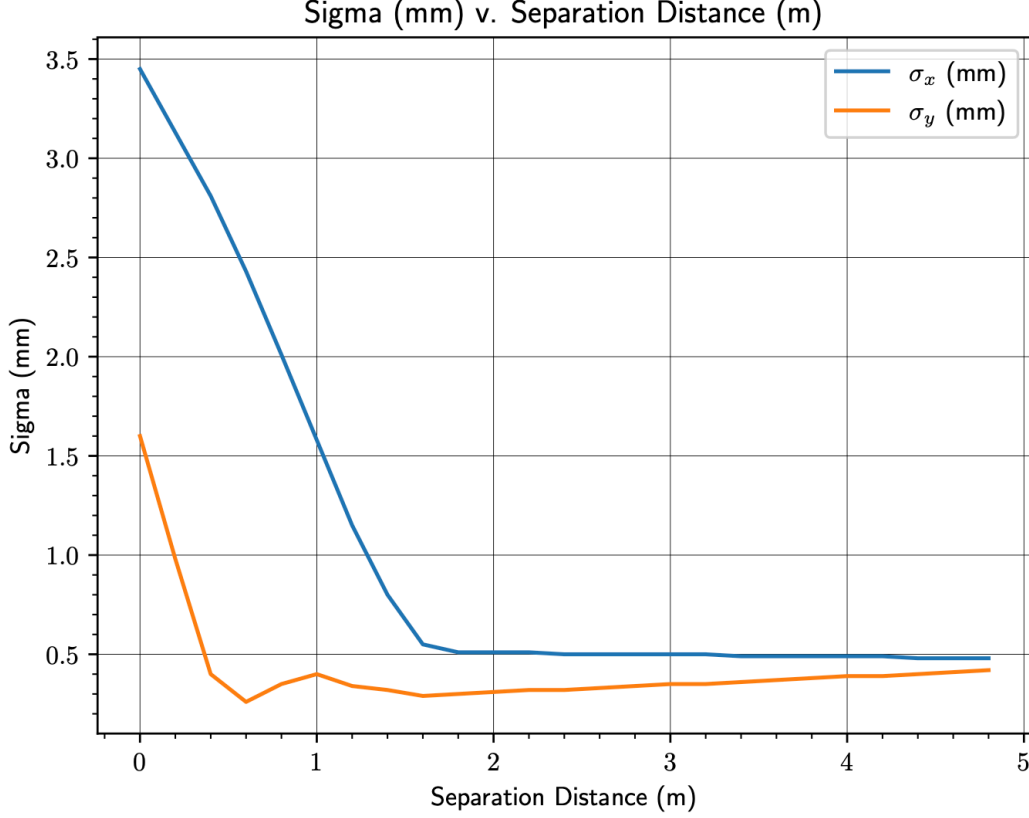


Figure 4: The σ_x and σ_y as a function of separation distance with the focus of PPE146 at 492.5 m and the focus of PPE156 at 536.5 m. One can see a clear decrease in σ until around 1.8 m where the values begin to plateau.

which the rest of the values begin to climb again, as demonstrated at a 4.8 m separation (see Fig. 5).

Naturally then, the separation distance is chosen to be 4.2 m. It is also important to note at this point that MAD-X does not include particle-matter interactions, but from a linear optics point of view, the optimal spacing is between 4 and 4.5 m.

3.3 Final Design

Table 2: Initial parameters for MAD-X simulations.

σ_p	0.00514748
ϵ_x	2×10^{-7} m
ϵ_y	5×10^{-8} m
β_x	10 m
β_y	10 m

Now, the final design is chosen. A doublet with a 4.2 m separation with the entrance of the first placed at 521.59 m. The parameters used to identify these conditions are provided in Table 3.3.

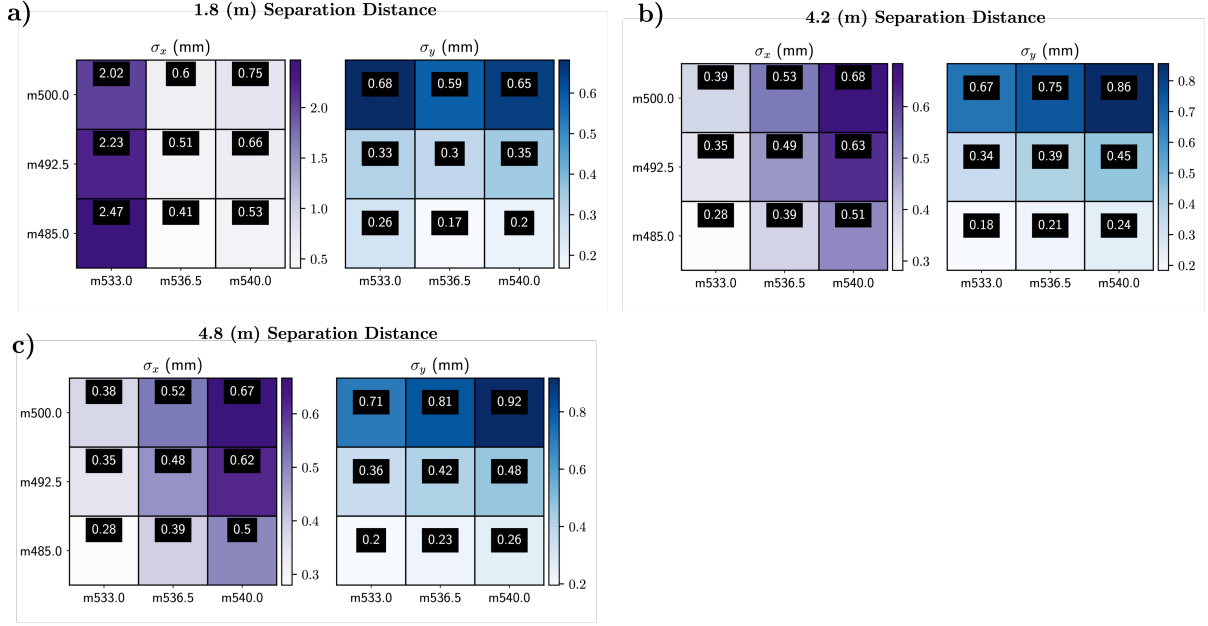


Figure 5: Tables generated showcasing the calculated sigma for different separation distances. The x -axis is the location of the focus in the PPE156 user zone, with the y -axis as the focus in the PPE146 user zone.

The σ_p value is the momentum spread, derived from the maximum value of the \mathcal{R}_{36} matrix element, which takes place directly after the first horizontal bend where the \mathcal{R}_{16} and \mathcal{R}_{26} terms are 0. The XCSH.041.128 collimator defines the momentum spread and in the nominal optics used, the value of $\mathcal{R}_{36} = 1.9426(\frac{m}{100\%})$, combined with a full collimator opening of ± 10 mm, gives a momentum spread of 0.00515% using the following unit conversion on the matrix element.

$$\left(\frac{100\%}{1.9426 m}\right) \left(\frac{1 m}{1000 mm}\right) \left(\frac{10 mm}{1}\right) = 0.00514748\%$$

The emittance values are taken from a previous BDSIM simulation and the β values are from a previous fit of measured σ values of the beamline.

To ensure that the beam does not scrape the sides of the beam pipe a condition is added that the radius of the magnet apertures must be greater than 5σ of the beam in accordance with the acceptance. The aperture radii are 40 mm, so adding this condition, one finds that β_x must not exceed 320 m and β_y must not exceed 1280 m. However, to aid the investigation a factor of 2 higher values was considered at 620 m for β_x . These limitations are assumed for the following discussion.

With the current configuration, one can achieve a simultaneous focus in PPE146 (485 m) and PPE156 (533 m) with $\sigma_x = 1.60$ mm, $\sigma_y = 0.26$ mm, $\sigma_x = 0.25$ mm, and $\sigma_y = 0.28$ mm respectively. Note that in the above case, the dispersion at the PPE146 focus is not completely eliminated to achieve this incredibly small beam spot. One can eliminate dispersion, however, it results in a larger spot size at 156 and it is more relevant to know the smallest spot one can achieve here. For foci in PPE156, the currents of Q17 and Q18 range from 282:250 A and 416:294 A.

Without the new doublet, a focus in the same place has $\sigma_x = 3$ mm and $\sigma_y = 0.97$ mm. With the new doublet, σ_x is 12 times smaller and σ_y is 3.46 times smaller. This results in a total reduction in area of 41.52.

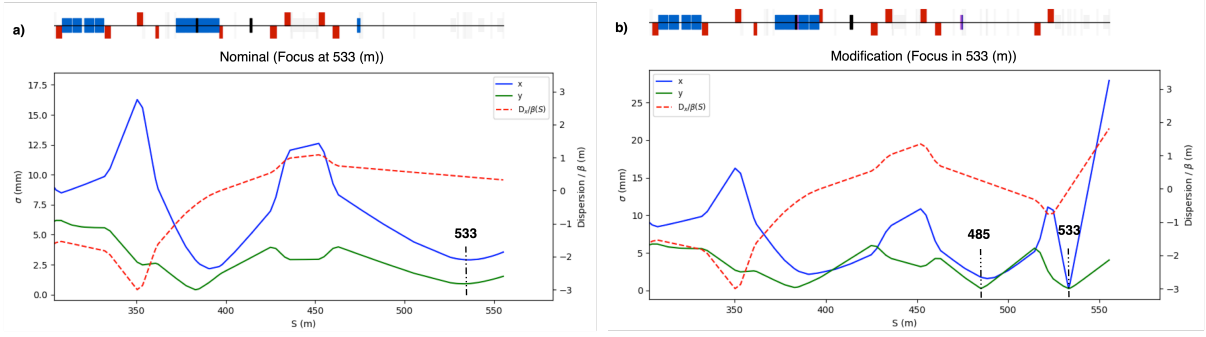


Figure 6: (a) The σ of the nominal optics focused at 533 m (b) The σ of the modified optics with a focus at 485 m and 533 m

4 Modeling

4.1 Verification

Using the doublet solution, a model was created in BDSIM which was used to predict how the beam will look at different points along the line, taking into account particle-matter interactions. As stated previously, the way MAD-X is implemented does not include these effects on the beam. One of these effects, which is certainly relevant to the applications, is that of multiple scattering due to the 50 m of air at the end of the beamline. First, the contribution of multiple scattering in air to our beam can be estimated, providing useful information and a nice sanity check that BDSIM agrees with the theoretical predictions.

Beginning with Eqn. 5 and identifying the relevant quantities for the estimation leads to a momentum of $120 \text{ GeV}c^{-1}$ and a Lorentz $\beta = 0.999939$. Additionally, $z = 1$, $x = 50 \text{ m}$, and $X_0 = 303.90 \text{ m}$. Substituting these into Eqn. 5 one find that $\theta_0 = 44.48 \mu\text{rad}$. Furthermore, the distribution for the radius from the above result can be determined using Bethe's approximation [3]:

$$y_{plane}^{rms} = \frac{1}{\sqrt{3}}x\theta_0 \quad (12)$$

One finds that $y_{plane}^{rms} = 1.284 \text{ mm}$. To compare this to BDSIM predictions, a simple model was created, constructing a 50 m target out of air, through which a beam with zero transverse size and divergence was sent, enabling solely electromagnetic physics.

The angular distribution of particles from 10,000 events is shown in Fig. 7. Comparing the simulation and theoretical results, there is good agreement between the two situations, as the approximation is good to within 11%, which is well within the range of the simulation. It is likely that the discrepancy between the two results would decrease as the number of simulated particles increases. From these findings, one can quite confidently say that the simulations are accurate, and move forward with the simulations.

Now that the configuration of quadrupoles is determined, the BDSIM model can be created. Luckily, there is a pre-existing model of the H6 beamline. To utilize this model and be sure of its validity, a few preliminary steps are required. First, the model must be verified and ensure that it is actually representative of the lattice. This was done by comparing the current model with the MAD-X sequence and cross-checking with CERN's Geographic Information System (GIS). This process revealed a few faults within the model, namely the areas inside and outside of the vacuum. There accuracy of these areas are of utmost importance as the multiple scattering throughout the line is crucial to the model and must be representative of the actual situation. Secondly, the collimator settings must be confirmed. These settings can be found in Table 4.1.

To validate the construction of the model as well as the strength of the prepared field maps in each magnet, a Gaussian beam is tracked through the lattice with only magnetic tracking

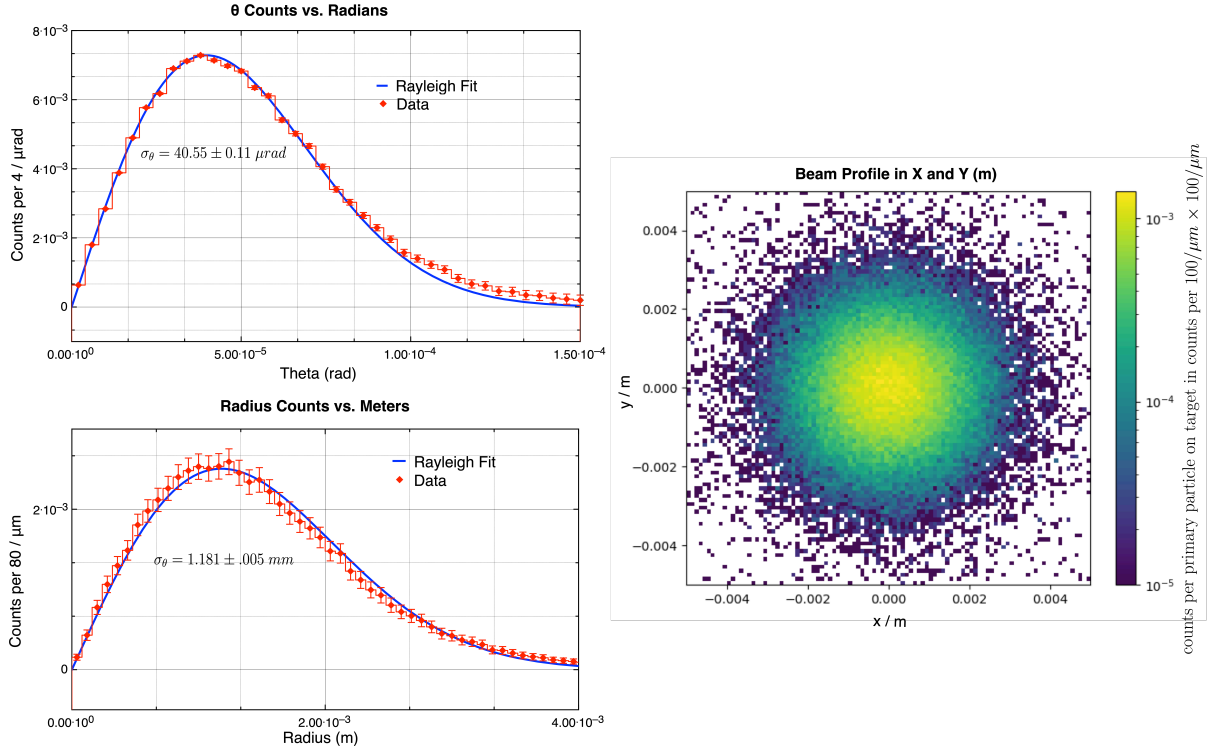


Figure 7: Distributions of scattering angle and radius with fit and sigma after 50 m of scattering in air. Included is a two dimensional histogram of the beam after multiple scattering.

physics activated. In other words, there was no scattering, interactions, or decay. The optical parameters are then calculated and compared with that of MAD-X. Whilst this is not the exact beam in reality, it allows comparison between MAD-X and tracking in BDSIM. As shown in Fig. 8, good agreement was found between optical parameters derived from tracked distributions and that of MAD-X.

Notably, at the end of Fig. 8 (a) one can observe some oscillations around the MAD-X prediction. This is a natural side effect of having a finite number of samples. The particles are sampled from a Gaussian distribution so there will always be slight deviations from the theoretical distribution. One way this manifests itself is in an offset mean. This will result in a beam distributed such that it is slightly offset from the reference orbit. The beam will then oscillate back and forth across the orbit, matching the exact behavior shown. This deviation would decrease as the number of samples increased.

With a validated model, a more realistic beam distribution can be simulated with a complete set of physics processes used. In reality, the beamline has a high attenuation ratio, of 10^{-7} , from protons on the target, so the simulation was split into two parts for greater computational efficiency. Firstly, a simulation of the protons on target up to the end of the TAX was done. The data from this simulation was reduced (‘skimmed’) for only events where at least one particle came through on the H6/H8 side of the TAX exit face. Secondly, a simulation of only these select events was launched into the H6 beamline model.

The output of these simulations can then be used as inputs for the rest of the line, increasing the efficiency of the entire procedure dramatically. Furthermore, the speed of the simulation can be increased by making appropriate energy cuts and filtering down particles by making a cut in physical space. This is important as the distribution files include particles from the TAX intended for the H8 beamline, which accepts momentums of 180 GeVc^{-1} , along with other particles of incorrect momenta and position, which will never make it down the beamline. These cuts are applied for energies of 10 GeV and in the x and y dimensions of $\pm 50 \text{ mm}$ and ± 30

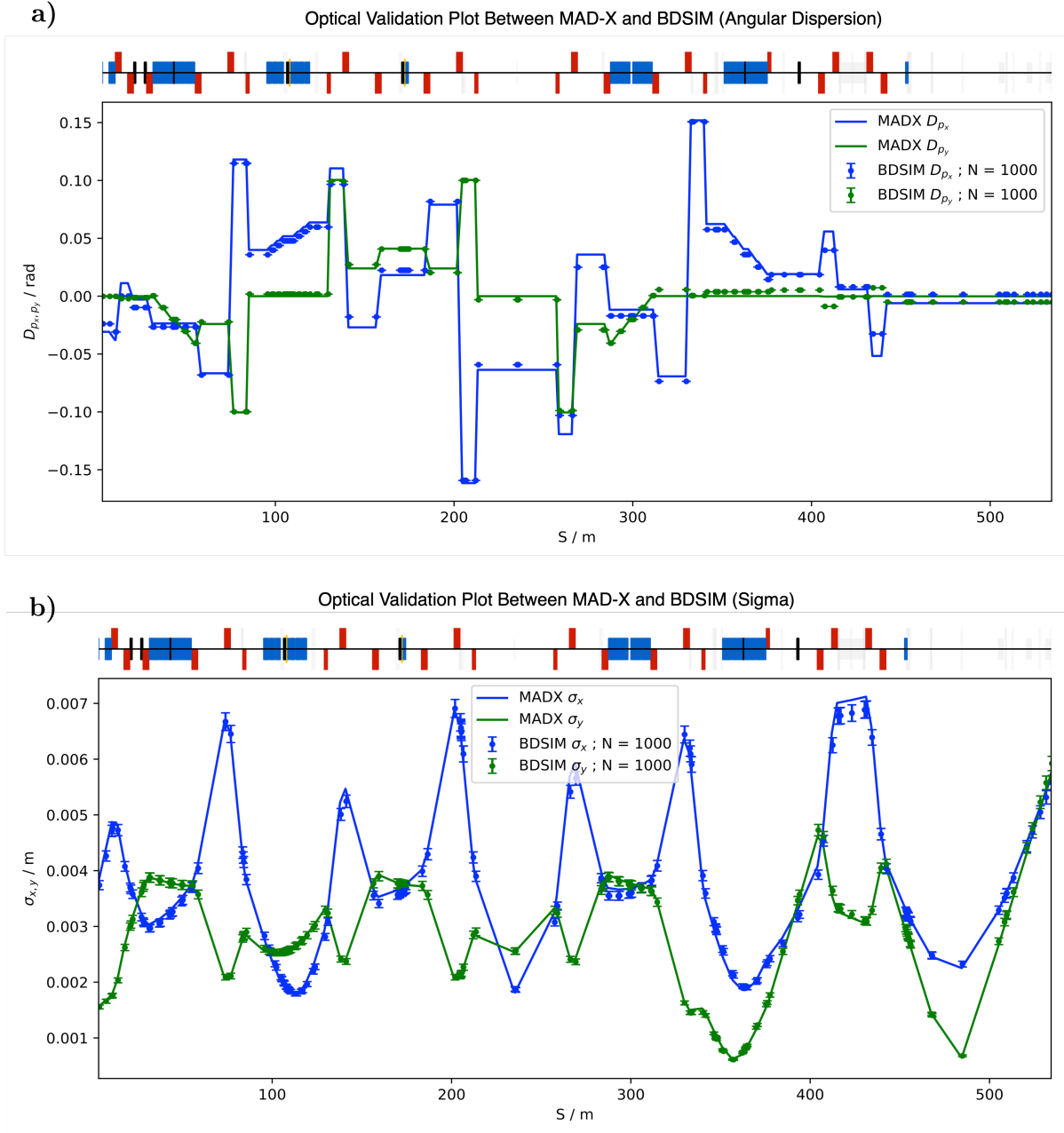


Figure 8: **(a)** The optical validation plot comparing MAD-X and BDSIM models with respect to angular dispersion, showcasing clear oscillation around the reference orbit. **(b)** The optical validation plot comparing MAD-X and BDSIM models with respect to sigma.

mm respectively⁴.

As one can see in Fig. 9, candidate particles with the correct momentum which are positioned correctly to enter the H6 beamline are well within the bounds set for the cuts. The particles not included in the bounds are ignored and computation time is decreased.

4.2 Predictions & Simulation Results

Now that the beamline has been simulated, the results can be analyzed, beginning with the spectrum in momentum of the particles in the beam. There are two places of particular in-

⁴Note that these bounds are applied to the center of the beam pipe after it is offset from the coordinate system in the figure.

Table 3: Nominal collimator settings for H6 beamline.

Collimator	Horizontal	Vertical
XCSH.043	± 3 mm	± 50 mm
XCSV.047	± 50 mm	± 3 mm
XCSH.064	± 3 mm	± 50 mm
XCHV.128	± 20 mm	± 10 mm
XCHV.192	± 20 mm	± 20 mm
XCSV.384	± 50 mm	± 20 mm
XCSH.414	± 20 mm	± 50 mm

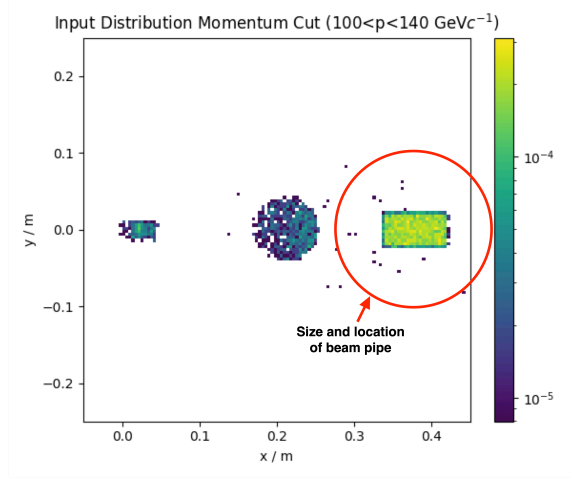


Figure 9: The input distribution fed into the line, showing only particles between 100 and 140 GeVc^{-1} . Overlaid on top is the size and location of the beam pipe for the H6 beamline.

Table 4: Number of events throughout steps of simulation. One event corresponds to one proton on target.

	Description	Value
Simulated	Protons on Target Simulated	5.836×10^9
	Skimmed Events after TAX	3.659×10^8
	# Events at XSCI.225	9.538×10^7
	# Particles at XSCI.225	1202
	# Particles at End of Vacuum	1096
	# Particles at End of Line	991
	Per-proton rate	1.70×10^{-7}

terest, the end of the vacuum and the end of the beamline. Investigating these two points simultaneously will provide insight into the effect of the air on the beam as well as the actual constitution of the beam itself.

Fig. 10 (a) shows the makeup of the beam right after the vacuum ends at the 488 m mark. As one can see, there are a few positrons, but the beam is predominantly composed of pions and protons - each contributing roughly half. Additionally, the majority of these particles are comfortably contained within $\pm 0.5 \text{ GeVc}^{-1}$.

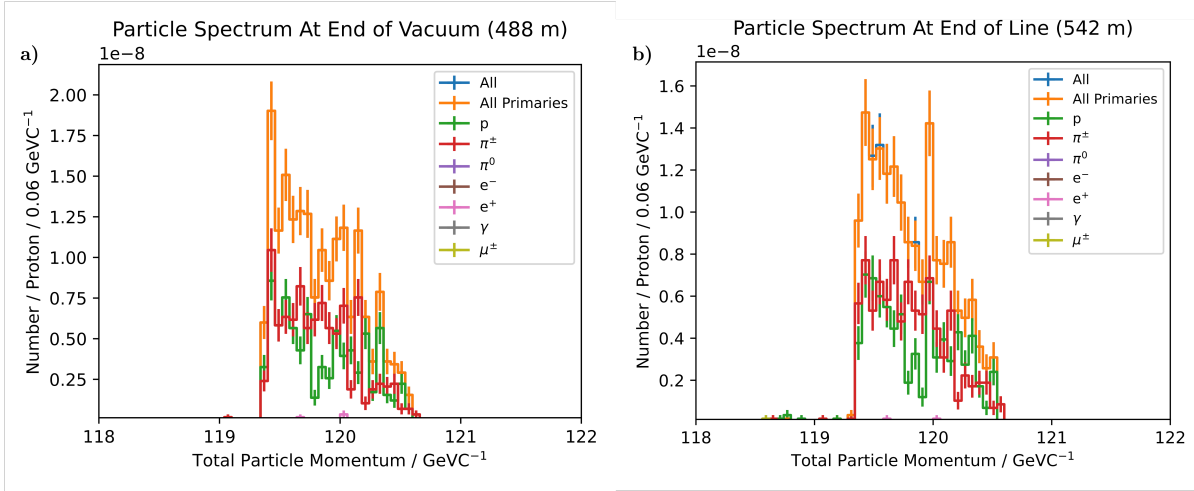


Figure 10: **(a)** The spectrum of particles in momentum at the end of the vacuum. **(b)** The spectrum of particles in momentum at the end of the line.

Now, at the end of the line, after multiple scattering in air, Fig. 10 (b) shows a greater diversity in momenta and particle type, adding some muons to the mix. Additionally, the momentum spread increases, with more particles having a lower momentum. In fact, one can see that the entirety of the spectrum has shifted to lower momenta. This matches expectations as the interactions with air would cause the particles to lose energy, and consequently, momentum.

Additionally, counting the number of particles that pass through points along the beamline provides the rate of protons per spill and the rate per proton on target. Assuming a spill size of 40×10^{11} protons on the T4 target with these collimator settings and target length results in a rate per spill of 6.80×10^5 for a rate per proton on target of 1.70×10^{-7} . These agree well with operational experience. More of these details can be seen in Table 4.2.

The same optical calculation (using the rebdsim tool) can be used on this more realistic data to see the variation in beam size and emittance along the beamline, shown in Fig. 11.

At the beginning of the line one can see that the emittance varies wildly, predominantly after the collimators - the black elements in the machine lattice. This makes sense as the collimators actively change the shape of the beam, and thus the emittance. The beam gets cut down and the emittance becomes essentially constant. Once this happens, the beam can be thought of as relatively Gaussian.

After the last collimator, the average value of the emittance and its associated error can be computed once the beam is cut down. These values are $1.68 \times 10^{-6} \pm 0.85 \times 10^{-6} m$ and $9.86 \times 10^{-7} \pm 5.8 \times 10^{-7} m$ for ϵ_x and ϵ_y respectively. One can notice quickly that our error is huge for these results. This can be understood simply by considering the huge attenuation that occurs throughout the line. As a result, only a thousand particles end up making it through the line for 100 million particles that make it through the TAX. With more time and simulation, the error can be reduced by increasing the number of particles that make it to the end.

With this simulation, we can now predict what the beam size will be at the focus. In this case, the focus is located at the 505 m mark. Fig. 12 displays the distribution of particles and the relevant sigmas at the nominal focus. Additionally, Fig. 12 (c) showcases the two dimensional histogram at that point. We find a σ_x of 2.0 ± 0.0489 mm and a σ_y of 0.759 ± 0.0201 mm.

4.3 Modification Simulation

The beamline can now be modified with the new solution and an estimation of the beam spot at the focus can be determined. Luckily, most of the beamline remains the exact same between this simulation and the prior one. So, one can take a sample from the previous results from right

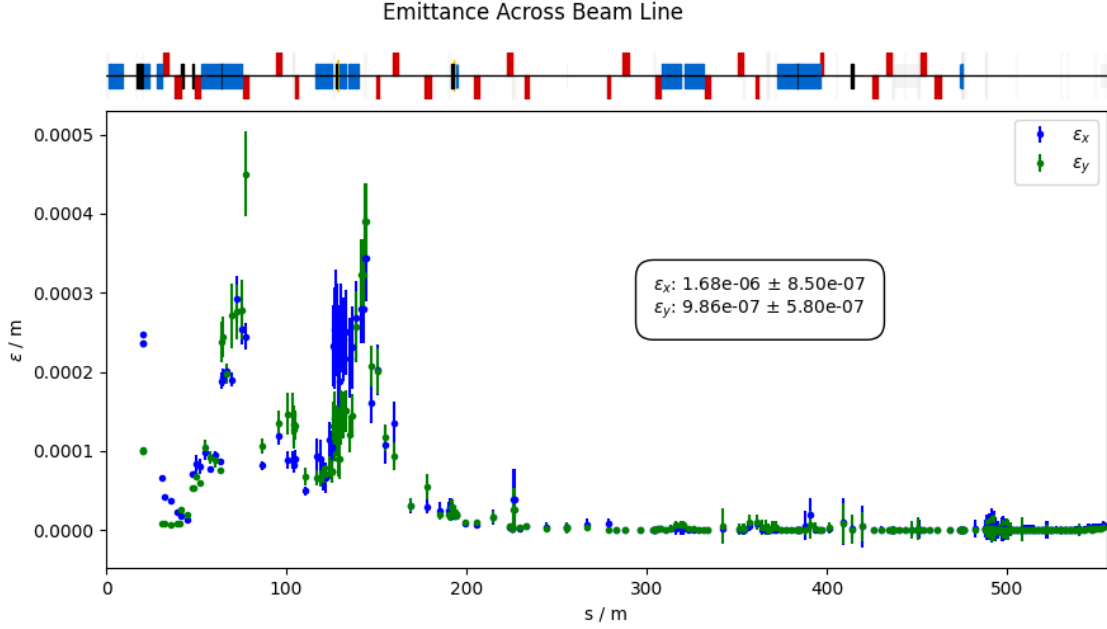


Figure 11: The emittance calculated across the line. The emittance at the end of the line is included in the text box.

before the beamline changes, and fire it down the line. This foregoes a lot of the computation time, and results are obtained much faster.

Sending the distribution from the previous simulation down the new model 10 times over results in the predicted focus displayed in Fig.13. Applying the correct scaling factor provides the expected rate per primary proton on target.

The simulated beam spot has a predicted σ_x of 0.247 ± 0.00413 mm and a σ_y of 0.905 ± 0.0153 mm, which is already smaller than the nominal focus at 505 m, which only gets larger as one attempts to focus it further down the beamline (i.e. at 533 m).

5 Experimental Results

5.1 Taking Data

To compare with simulation, some beam time was provided in H6. Python scripts were written based on the BE-EA-LE Python package *eaoperation* that allows control of individual magnet currents. Another provided package, *eamagparam*, was used to convert normalised strengths from MAD-X output to currents for given magnets for a given momentum, including the particular polarity of each magnet installed.

The number of particles was given by calibrated scintillators along the beamline, with the CESAR interface pictured in Fig. 14. Beam profiles were recorded from a combination of analogue and delay wire (ionization) chambers that give 1D profiles in either the horizontal or vertical direction.

Before each scan was taken, the settings for the beamline were confirmed to be nominal and that the collimators matched the settings in Table 4.1.

A number of scans were completed, including moving the smallest focus across the PPE146 and PPE156 user zones by varying three quadrupoles and seven quadrupoles. Moreover, a profile of the beam was acquired with which to compare to the simulations. In addition, a scan was completed in which a singular quad was varied to move a focus in the x and y dimensions. Using this data, the procedure outlined in Nevay et al. [10], was followed to determine the

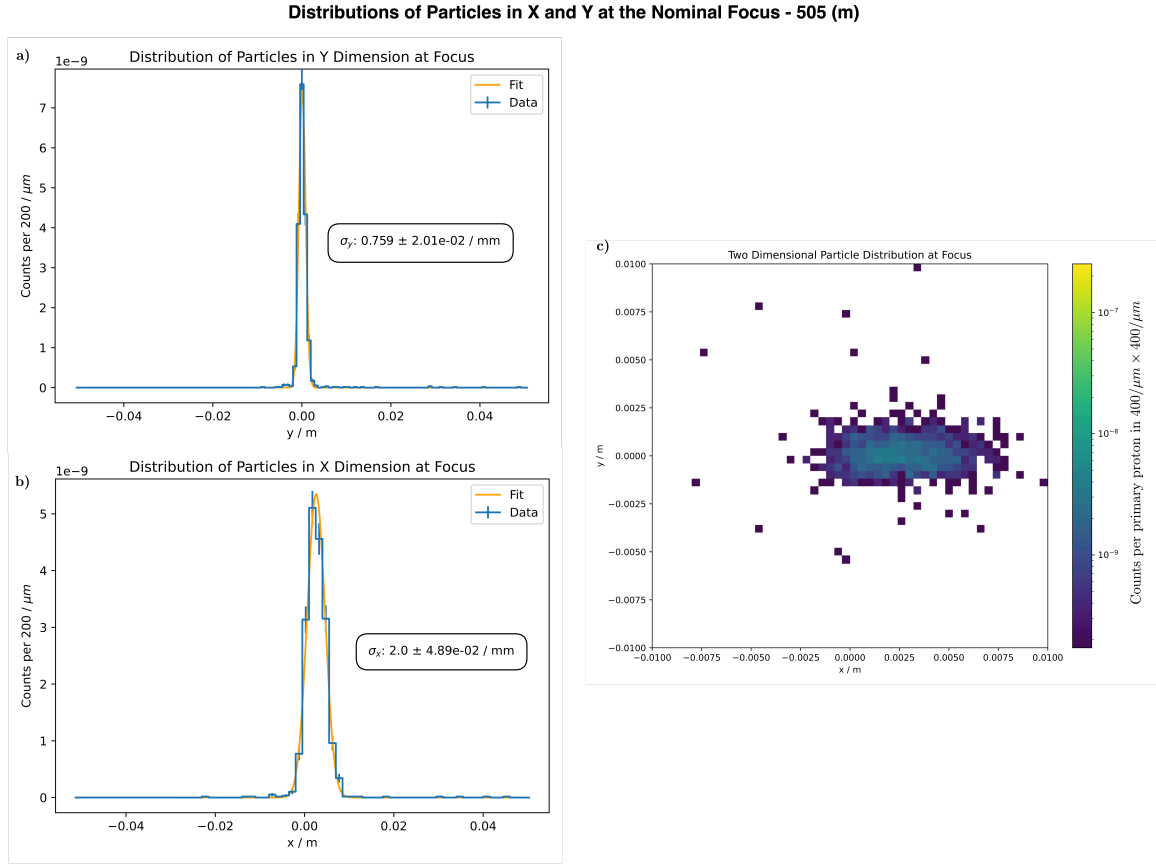


Figure 12: The distributions of particles histogrammed per primary proton on target for the nominal configuration. **(a)** A histogram of the distribution of particles in the y dimension at the nominal focus of 505 m. **(b)** A histogram of the distribution of particles in the x dimension at the nominal focus of 505 m. **(c)** A two dimensional histogram of the particles at the nominal focus, showcasing how the beam looks at this point in the line.

emittance of the beam.

5.2 Comparisons

The data acquired from the beamline itself in its nominal state can be compared to the nominal simulation. To do this, the sigma of the beam at each different wire chamber was calculated and compared to the simulation. For this, three different sets of data were used: the simulated data, the measurement taken for this project, and measurements taken previously.

As one can see in Fig. 15, at the first four points, there is a high agreement as to the size of the beam, with all three points being clustered around one another. Additionally, they agree - to an extent - with the MAD-X prediction. This is expected as it is a MAD-X prediction for a given set of initial conditions which may not be accurate, still it is a useful tool. The remaining three measurements, however, show unusual behavior.

Even between the two experimental measurements there exists large dissent. Another independent measurement at 542 m, made by EP Pixel, a user in the zone, recorded a beam spot smaller than that measured at 532 m. This means that somehow, if the 532 m measurement is to be believed, the beam became convergent after 532 m, which is highly unlikely. The sigma of the previous measurement, however, appear to match up more closely to this independent measurement.

Distributions of Particles in X and Y at 533 (m) with Additional Doublet

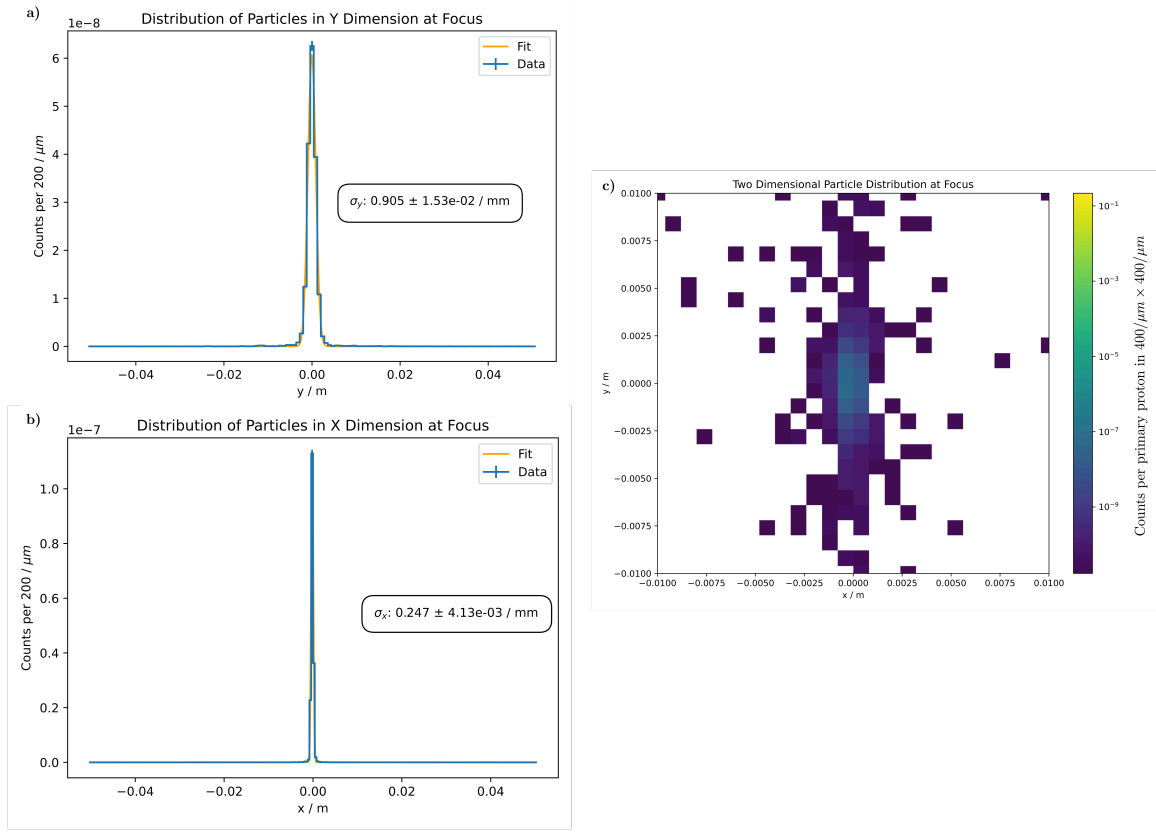


Figure 13: The distributions of particles histogrammed per primary proton on target for the modified configuration with two new quadrupoles. (a) A histogram of the distribution of particles in the y dimension at 533 m with two new quadrupoles. (b) A histogram of the distribution of particles in the x dimension at 533 m with two new quadrupoles. (c) A two dimensional histogram of the particles at a focus of 533 m, showcasing how the beam looks at this point in the line.

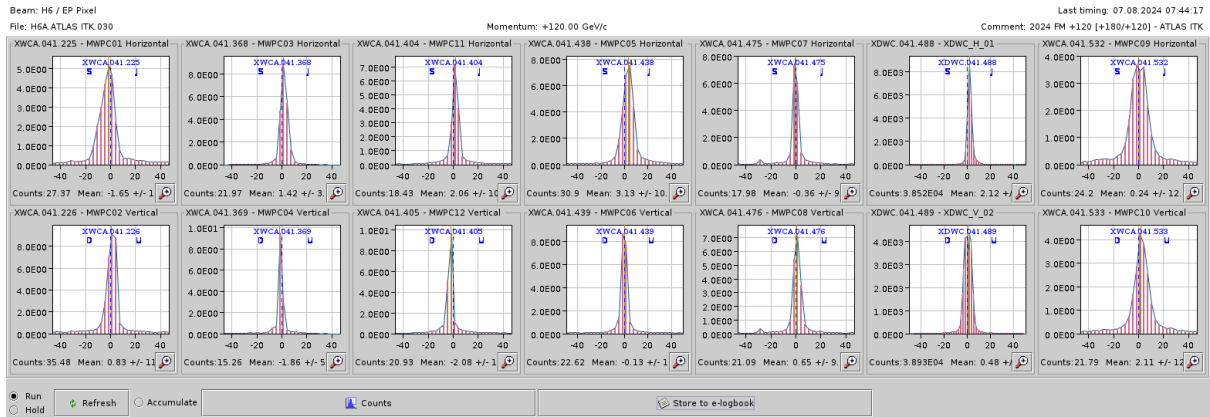


Figure 14: Image of the CESAR interface showing beam profiles along the H6 beamline. Horizontal profiles are shown on the top row and vertical on the bottom row.

5.3 Emittance

To determine the emittance of the beam, one must move a focus in one dimension across a wire chamber, from which they can identify the sigma of the beam and the emittance in

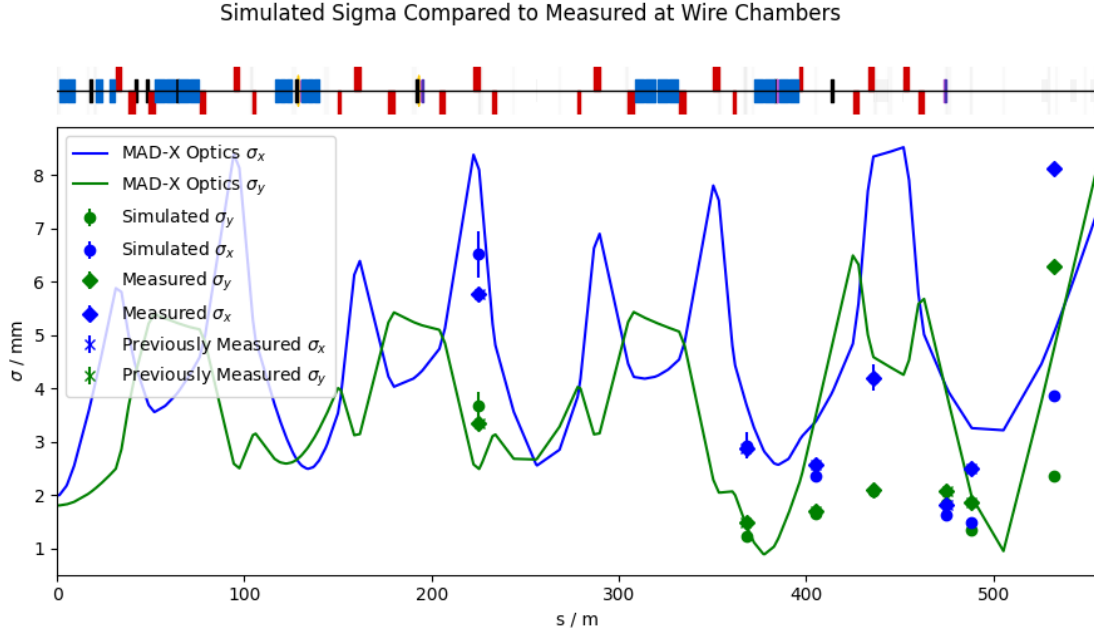


Figure 15: The beam size as predicted by simulation and measured on two different occasions. Included as well is a MAD-X prediction of the sigma. One should note that the MAD-X prediction is fitted to the previous measurement and uses the emittances calculated in §5.3.

that dimension. To do this, a two step procedure was followed, which involves the last two quadrupoles in the lattice. The first quadrupole - called Q15 - is at 453 m and focuses in the x direction and defocuses in the y dimension while the quadrupole at 461 m (Q16) does the opposite. The procedure to measure the emittance contains two major steps. First, the quadrupole which defocuses the relevant dimension was varied about a general focus at the wire chamber in the other dimension. Then, the other quadrupole was varied to shift the relevant focus across the same chamber.

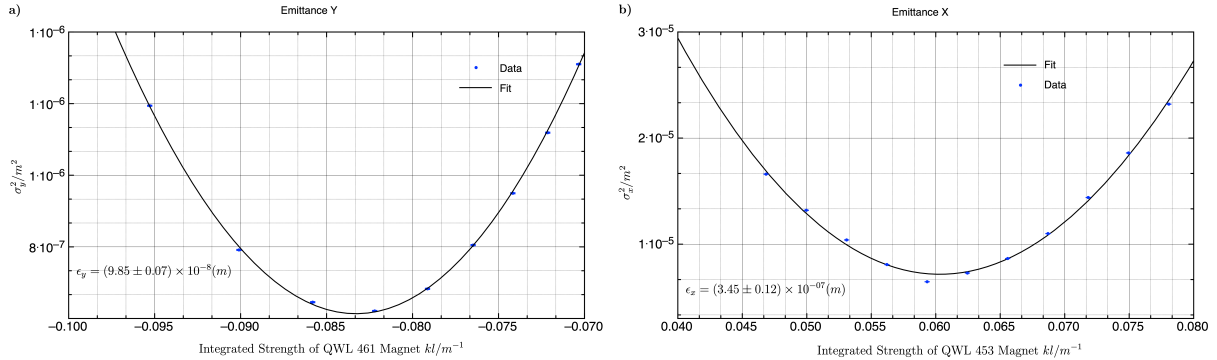


Figure 16: Emittance determined from scans where one upstream quadrupole is varied to shift each focus respectively.

One can imagine then if there is a stationary chamber constantly measuring the size of the beam, as a focus moves across it, it will create a parabolic shape as shown in Fig. 16. Eqn. 13 from Nevay et al. was used to fit the free parameters a , b , and c and determine the emittance.

$$\sigma_i^2 = a[m_{11}(kl) + bm_{12}(kl)]^2 + cm_{12}^2(kl) \quad (13)$$

The emittance is given by $\epsilon_i = \sqrt{ac}$. Emittances of $(9.85 \pm 0.07) \times 10^{-8}$ and $(3.45 \pm 0.12) \times$

10^{-7} for ϵ_y and ϵ_x respectively were determined. The value for ϵ_y lies within the range of those calculated from the simulation, however, ϵ_x does not. This is likely because of the low number of samples.

6 Summary and Outlook

A new configuration of quadrupoles, utilizing pre-existing magnets and wiring infrastructure, which will allow the creation of simultaneous foci in user zone PPE156 and PPE146 was determined. With this new configuration the beam spot can be reduced by a predicted 40 times. This results in more flexibility within the line and increases the “usable” beam for smaller sensors.

A full model of the H6 beamline was created and validated. Through the use of a two stage simulation, the beamline was simulated from start to finish, allowing predictions regarding the spectra, rate, emittance, and size of the beam to be made throughout the line.

Additionally, several scans of the wire chambers in the line were taken and the data was used to determine the emittance and size of the beam at various points.

The simulations display a high level of consistency with the measurements. There is some interesting divergence of the sigma measurements at the end which is currently unexplained and further measurements are needed to increase the accuracy of the comparisons and elucidate the issue. These measurements may take some time as, per the time of writing, there is a copper block in PPE146 which further scatters the beam and so is not representative of the nominal optics in PPE156.

Due to the severe attenuation ratio, only ~ 1200 particles were transmitted in the simulation for 100 million events. Further simulations would improved these statistics given more time. The rebdsim optics calculation code was written to analyse all particles together in a serial fashion and therefore it cannot be parallelised across all of the optics files. Simultaneous analysis of multiple files showed a computation time of approximately 1 CPU-hour per million events. To ensure the final 1200 particles are analysed would require 100 million events to be analysed. Practically, 18 million events were analysed given the time constraint.

Further simulations with greater statistics will identify and solve differences observed between the simulation model and measured profiles. Further measurements to fully capture the minimum of the focus scan will also confirm the emittance measurement in the horizontal. It was possible that the upstream magnets were not configured correctly or there was an error in procedure that lead to the difference which could be confirmed with further measurements.

In addition, good agreement with overall transmission was found as well as reasonable agreement with beam size.

A solution was proposed for a new doublet placed at the end of PPE146 to create a secondary focus in PPE156. This would reduce the beam area by a factor of 40 on today’s operation and consequently reduce the data taking time for minute silicon detectors at the end of the beamline by a similar factor.

Overall, a better understanding of the H6 Secondary Beamline has been developed and along with tools to gain a futher understanding of how it truly behaves, which will only be improved upon in the future.

References

- [1] S. Agostinelli et al. GEANT4—a simulation toolkit. *Nucl. Instrum. Meth. A*, 506:250–303, 2003.
- [2] D. Banerjee, J. Bernhard, M. Brugger, N. Charitonidis, N. Doble, L. Gatignon, and A. Gerbershagen. The North Experimental Area at the Cern Super Proton Synchrotron. 2021.
- [3] H. A. Bethe. Molière’s theory of multiple scattering. *Phys. Rev.*, 89:1256–1266, Mar 1953.
- [4] Ilias Efthymiopoulos. Target Station T4 Wobbling - Explained. 2003.
- [5] L Gatignon. Magnets kit for the experimental areas of the cern ps/sps complex, Feb 2004.
- [6] Anthony Gerrard and James M. Burch. *Introduction to matrix methods in optics*. Dover Publications, Inc, 1994.
- [7] H Grote and F Schmidt. MAD-X: An Upgrade from MAD8. 2003.
- [8] Wolfgang Hillert. Transverse linear beam dynamics, 2021.
- [9] Gerald R. Lynch and Orin I. Dahl. Approximations to multiple coulomb scattering. *Nuclear Instruments and Methods in Physics Research Section B: Beam Interactions with Materials and Atoms*, 58(1):6–10, 1991.
- [10] L. J. Nevay, S. T. Boogert, P. Karataev, K. Kruchinin, L. Corner, D. F. Howell, R. Walczak, A. Aryshev, J. Urakawa, and N. Terunuma. Laserwire at the accelerator test facility 2 with submicrometer resolution. *Phys. Rev. ST Accel. Beams*, 17:072802, Jul 2014.
- [11] L.J. Nevay, S.T. Boogert, J. Snuverink, A. Abramov, L.C. Deacon, H. Garcia-Morales, H. Lefebvre, S.M. Gibson, R. Kwee-Hinzmann, W. Shields, and S.D. Walker. Bdsim: An accelerator tracking code with particle–matter interactions. *Computer Physics Communications*, 252:107200, 2020.
- [12] Helmut Wiedemann. *Particle accelerator physics*. Springer International Publishing, 2015.